

Research Article

Experimental Study of a Low-Specific Speed Francis Model Runner during Resonance

Einar Agnalt ¹, Petter Østby ^{1,2}, Bjørn W. Solemslie ¹ and Ole G. Dahlhaug¹

¹Waterpower Laboratory, Department of Energy and Process Engineering,
NTNU—Norwegian University of Science and Technology, Trondheim, Norway

²Rainpower AS, Kjeller, Norway

Correspondence should be addressed to Einar Agnalt; einar.agnalt@ntnu.no

Received 10 September 2018; Revised 8 November 2018; Accepted 28 November 2018; Published 23 December 2018

Academic Editor: Rui Moreira

Copyright © 2018 Einar Agnalt et al. This is an open access article distributed under the Creative Commons Attribution License, which permits unrestricted use, distribution, and reproduction in any medium, provided the original work is properly cited.

An analysis of the pressure in a runner channel of a low-specific speed Francis model runner during resonance is presented, which includes experiments and the development of a pressure model to estimate both the convective and acoustic pressure field from the measurements. The pressure was measured with four pressure sensors mounted in the runner hub along one runner channel. The mechanical excitation of the runner corresponded to the forced excitation from rotor-stator interaction. The rotational speed was used to control the excitation frequency. The measurements found a clear resonance peak in the pressure field excited by the second harmonic of the guide vane passing frequency. From the developed pressure model, the eigenfrequency and damping were estimated. The convective pressure field seems to diminish almost linearly from the inlet to outlet of the runner, while the acoustic pressure field had the highest amplitudes in the middle of the runner channel. At resonance, the acoustic pressure clearly dominated over the convective pressure. As the turbine geometry is available to the public, it provides an opportunity for the researchers to verify their codes at resonance conditions.

1. Introduction

Power plants with recently installed Francis runner have experienced breakdown after few running hours [1]. Some breakdowns are related to vibration and resonance of the runner. A resonance condition for a runner is known to have a frequency and a related shape with diametral modes (DMs) [2]. In low-specific speed runners, the main excitation force is found to be the rotor-stator interaction (RSI). The RSI excites the runner with a distinct pattern dependent on the number of runner blades and guide vanes [3–6]. Due to the phase shift of the pressure fluctuations in each runner channel, the overall pressure fluctuations in the runner create a pressure field with mean diametrical modes similar to the frequency response of the runner [7]. Hence, the verification of the frequency response of a runner is crucial to avoid operation at resonance.

The way of measuring frequency response found in the literature is with the use of accelerometers and strain

gauges, and the excitation methods found is pressure field excitation, impact excitation, or excitation with various vibration mechanisms as electronic muscles and shakers. The surrounding structure of the runner has high impact on the natural frequencies and damping; hence, the analysis should preferably be carried out with the runner mounted in the housing [3, 8]. Presas et al. analyzed the frequency response of a pump turbine while mounted in the housing, but the use of two electronic muscles was not sufficient to excite all modes [9]. Østby et al. performed a similar experiment but with six patches on a six-bladed model with good results. Major findings included that the modes with large movement of hub and shroud, the global modes, disappeared when the runner was mounted in the housing. The blade modes were minimally affected by the housing [10]. Valentin et al. analyzed the natural frequencies of a prototype turbine through impact excitation in air and later, pressure field excitation while in operation. Strain gauges and accelerometers were utilized to measure the

frequencies and the modal shape. The results included natural frequencies excited during startup and frequencies excited by random phenomena in part load and high load. By utilizing the excitation which naturally occurs in the operation of the runner, excitation complexity is reduced [11]. Several other studies focused on the frequency response and the added mass effect, mainly with measurements carried out with the runner not mounted in the turbine housing [12–17].

The objective of this paper is to investigate the use of pressure sensors to find the resonance frequency of a runner. RSI is used to excite a model of Francis turbine runner with forced excitations, and the mechanical response is measured with the pressure sensors mounted in one runner channel and one accelerometer mounted above one runner channel close to the inlet. In addition, to allow numerical research to verify their calculations, a model which separates the convective pressure field from the incompressible flow field and the acoustic pressure field from the acoustic-mechanical eigenmodes, have been developed. It produces useful estimates for the pressure fields, damping, and eigenfrequency which can be evaluated individually against the numerical calculations. This is a significant advantage as the researcher can verify each step of the calculation process and not only the final resulting pressure field. The turbine geometry in the current study is openly available through the Francis99 project and provides a unique opportunity for numerical researchers to verify their codes at resonance conditions [18].

2. Methods

2.1. RSI Excitation. The guide vanes create lift to direct the flow, and as a result, a circumferential repetitive pattern around the runner with zones of higher and lower pressure is created [19]. When the runner rotates, each runner channel is experiencing a varying pressure and velocity field depending on the position relative to the guide vanes. This variation of the inlet condition to the runner channels is the source of the fluctuation pressure found onboard the runner. Due to the different number of runner channels and guide vanes, the fluctuating pressure in different runner channels is phase shifted. As a result, the overall pressure onboard the runner, and thereby the forces acting on the runner, has a pattern of higher and lower pressure. Since the pressure in each channel fluctuates, the overall pressure pattern is rotating. This overall pressure field is known as the modal pressure field or the pressure spinning mode and can be expressed with the following [3, 20]:

$$mZ_b + nZ_g = k, \quad (1)$$

where m and n are the harmonic number for the runner pressure and guide vane pressure, respectively. The number of diametral modes is k , the number of blades is Z_b , and the number of guide vanes is Z_g .

The runner in the current study is equipped with $Z_g = 28$ guide vanes and $Z_b = 30$ runner blades. The excitation force for the fundamental guide vane passing frequency, $m = 1$ and $n = 1$, gives $k = 2$ diametral modes in the pressure field

and is illustrated by dividing a 28-period signal into 30 segments as shown in Figure 1.

The second harmonic of the guide vane passing frequency, $m = 1$ and $n = 2$, results in $k = 4$ and can be seen in Figure 2.

The deflection pattern of the runner is defined by the excitation from the pressure field. Each deflection pattern with diametral modes can have different deflection amplitudes for the blades, hub and shroud. The blade mode is a deflection pattern of the runner where the blades have the largest amplitude, while the disc mode is a deflection pattern of the runner where the hub and shroud have the largest amplitudes. Modes with high deflection of the hub and ring, disc modes, could have higher damping due to the surrounding water and structure in the housing compared to blade modes [10].

2.2. Experimental Setup. The Francis test rig available at the Waterpower laboratory, Norwegian University of Science and Technology, was used for the experimental studies as shown in Figure 3. The Francis test rig was equipped with all required instruments to conduct model testing according to IEC 60193 [21]. The runner in the current study was a bolted design with a 15 + 15 splitter and full-length blades. The number of guide vanes was 28, and the spiral casing was bolted through 14 stay vanes. The dimensionless specific speed of the runner was 0.07. The draft tube of the test rig was an elbow-type. The Francis turbine in the test section is shown in Figure 4 and the Hill diagram of the investigated runner is shown in Figure 5.

Measurements involving moving fluids can be severely influenced by the mounting method of the sensor [22]. For application where accurate flush mounting is possible, the uncertainty from mounting, i.e., related to hole size, transmission tubes and cavities will be neglectable [23]. The time and frequency response for the measurements are then only related to the dynamic properties of the diaphragm and the data acquisition (DAQ) chain [24]. In the current measurements, flush mounted sensors were selected to reduce uncertainty related to mounting method.

Figure 6 shows the locations of the onboard pressure sensor in the turbine (R1–R4) and the accelerometer (A). The pressure sensor sensing technology consists of a Wheatstone bridge with silicon strain gauges. The R1 and R2 sensors were Entran EPX sensors, and the R3 and R4 sensors were Measurements Specialties XPM5. In addition to the pressure sensors, a Brüel & Kjær 4397 accelerometer was utilized for reference measurement of the runner vibration. All of the sensors were mounted in the runner's hub, and the signals were amplified onboard and then transmitted through a slip ring before the connection to the DAQ system. The slip ring was a Penlink SRH-series for through-bore applications mounted on the shaft between the runner and the generator. A schematic presentation of the measurement system is shown in Figure 7.

2.3. Pressure Model. All pressure values presented were calculated as percentage of specific hydraulic energy of the

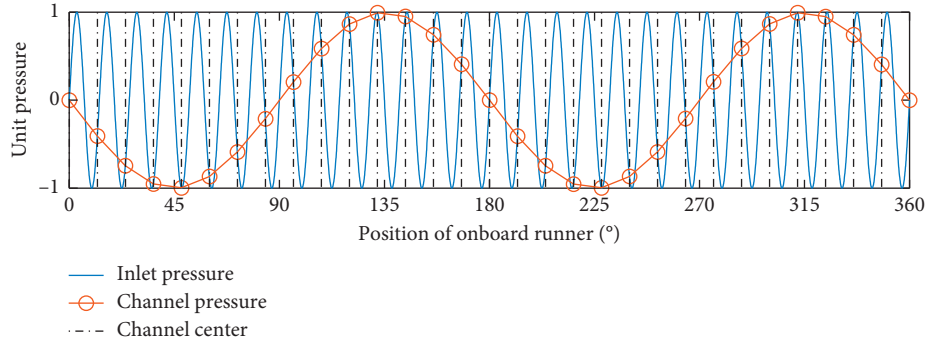


FIGURE 1: Instantaneous illustration of the DM2 excitation. A sinusoidal signal with 28 periods is divided into 30 equal segments. The intersection line for each segment represents the pressure in each of the 30 runner channels. By plotting a curve through the intersection points, the overall pressure with 2 diametral modes appears.

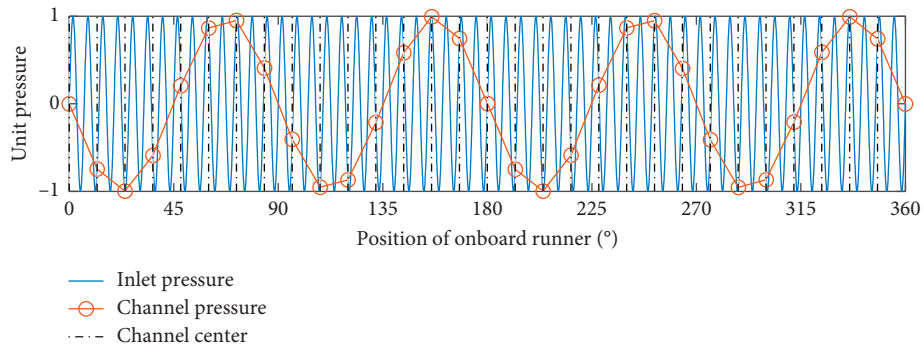


FIGURE 2: Instantaneous illustration of the DM4 excitation. A sinusoidal signal with 2×28 periods is divided into 30 equal segments. The intersection line for each segment represents the pressure in each of the 30 runner channels. By plotting a curve through the intersection points, the overall pressure with 4 diametral modes appears.

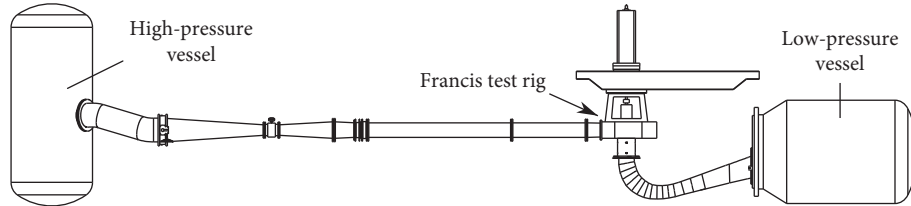


FIGURE 3: The Francis test rig, including the high- and low-pressure vessel.

machine ($E = gH$) and denoted p_E (%) as recommended by the IEC 60193 [21] where H is the net head. Fluctuating quantities are denoted with a tilde (\sim). The pressure fluctuations in the runner channel are assumed to be a linear combination of a convective (\tilde{p}_c) pressure from the flow field and an acoustic pressure from an excited acoustic-mechanical eigenmode in the runner (\tilde{p}_a). The total pressure fluctuation (\tilde{p}_t) in the channel is the sum of the convective and acoustic pressure as follows:

$$\tilde{p}_t = \tilde{p}_c + \tilde{p}_a \quad (\%E). \quad (2)$$

Both the dynamic convective pressure (\tilde{p}_c) and the dynamic acoustic pressure (\tilde{p}_a) can be modelled as transient waves with a real and an imaginary component. The convective pressure amplitudes are assumed to be proportional to the turbine head, and the relative phase angle between

each sensor, j , is assumed unchanging even with a change in runner speed; thus,

$$\tilde{p}_{c,j} = \tilde{p}_{cRe,j} + \tilde{p}_{cIm,j} \quad (\%E). \quad (3)$$

The acoustic pressure was modelled as the response of a coupled acoustic mechanical 2DOF system to accommodate higher modes while still limiting the number of unknowns in the model. As the fluid at the wall acts with the effect of added mass, the pressure has to be proportional to the frequency squared. A frequency proportionality $\omega_p = \omega/\max(\omega)$ factor is used where $\max(\omega)$ is the highest measured frequency. The amplification of the acoustic mode can thus be described as follows:

$$D(\omega, \zeta) = \frac{\omega_p^2}{(1 - (\omega/\omega_n)^2) + i \cdot (2 \cdot \zeta \cdot (\omega/\omega_n))} \quad (-), \quad (4)$$

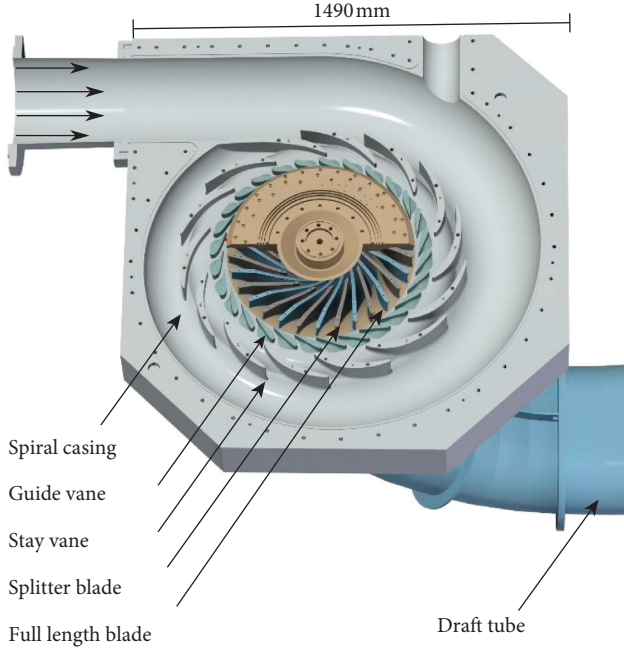


FIGURE 4: Three-dimensional view of the investigated Francis turbine.

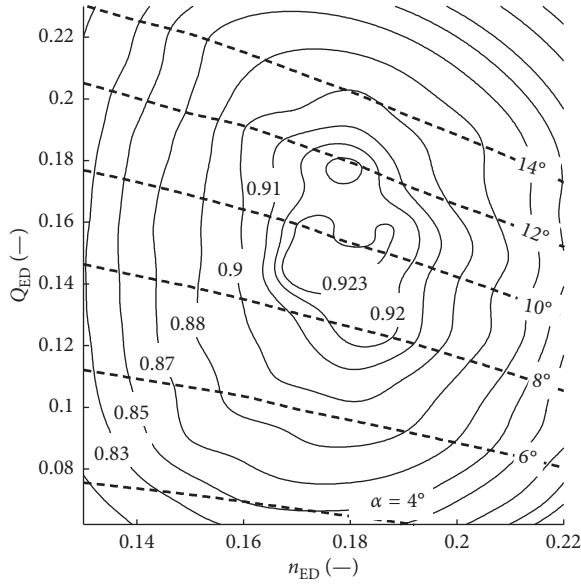


FIGURE 5: Hill chart of the investigated runner.

where ω denotes the excitation frequency, ω_n is the natural frequency of the excited eigenmode, and ζ is the relative damping factor. The acoustic pressure at each sensor, j , for the two normal modes in the system is thus described by the following equation:

$$\tilde{p}_{a,j} = (\Phi_{\text{Re},j} + i \cdot \Phi_{\text{Im},j}) \cdot D(\omega, \zeta) \Big|_1 + (\Phi_{\text{Re},j} + i \cdot \Phi_{\text{Im},j}) \cdot D(\omega, \zeta) \Big|_2 \quad (\%E). \quad (5)$$

Here Φ_j is the acoustic mode with a value for each sensor, j . Based on the measurements by Bergan et al. [25]

the damping is assumed to be proportional to the water velocity going through the runner.

$$\zeta = k \cdot \omega_p \quad (-). \quad (6)$$

The model has a total of 28 unknowns, 8 of which are for the complex convective pressure field, another 16 are for the complex acoustic pressure field, two are for the eigenfrequencies, and two are for the scaling constants k for the damping:

$$\begin{aligned} \tilde{p}_{t,j} = & (\tilde{p}_{\text{cRe},j} + i \cdot \tilde{p}_{\text{cIm},j}) \quad \text{Convective} \\ & + (\Phi_{\text{Re},j} + i \cdot \Phi_{\text{Im},j}) \cdot D(\omega, \zeta) \Big|_1 \quad \text{Mode 1} \\ & + (\Phi_{\text{Re},j} + i \cdot \Phi_{\text{Im},j}) \cdot D(\omega, \zeta) \Big|_2 \quad \text{Mode 2.} \end{aligned} \quad (7)$$

The accelerometer was modelled without the frequency squared in the amplification D , but with the same damping and natural frequencies giving another 6 unknowns. The convective part in the pressure was modelled as a constant part in the accelerometer.

$$D_a(\omega, \zeta) = \frac{1}{(1 - (\omega/\omega_n)^2) + i \cdot (2 \cdot \zeta \cdot (\omega/\omega_n))} \quad (-),$$

$$\begin{aligned} \tilde{a} = & (a_{\text{cRe}} + i \cdot a_{\text{cIm}}) \quad \text{Const} \\ & + (A_{\text{Re},j} + i \cdot A_{\text{Im},j}) \cdot D_a(\omega, k) \Big|_1 \quad \text{Mode 1} \\ & + (A_{\text{Re},j} + i \cdot A_{\text{Im},j}) \cdot D_a(\omega, k) \Big|_2 \quad \text{Mode 2,} \end{aligned} \quad (8)$$

With the accelerometer included in the fit, the total number of unknowns was 34.

2.4. Measurements. The frequencies for the forced excitation were controlled by changing the speed of the runner while changing the head to keep the speed factor (n_{ED}) around the best efficiency point (BEP). The results in this paper are based on the operational conditions shown in Table 1. To maintain similar flow conditions, all measurements were close to BEP. The flow was measured in the inlet pipe with an electromagnetic flow meter.

2.5. Calibration and Uncertainty. The uncertainty of the measurements was calculated from calibrations, vibration sensitivity, and repeatability of the measurements. Static calibration of the pressure sensors was initially done in an estimated pressure range for the measurements with a GE P3000 Series pneumatic deadweight tester as the primary reference. As the evaluation of the pressure amplitudes was a dynamic quantity, dynamic uncertainty was addressed. All components in the current pressure measurement chain, from the sensors to the data acquisition, were stated to have resonance frequencies above 10 kHz; hence, the dynamic uncertainty was assumed to be neglectable, and only repeatability and hysteresis from static calibration remained in the uncertainty evaluation [26]. A repeatability test was

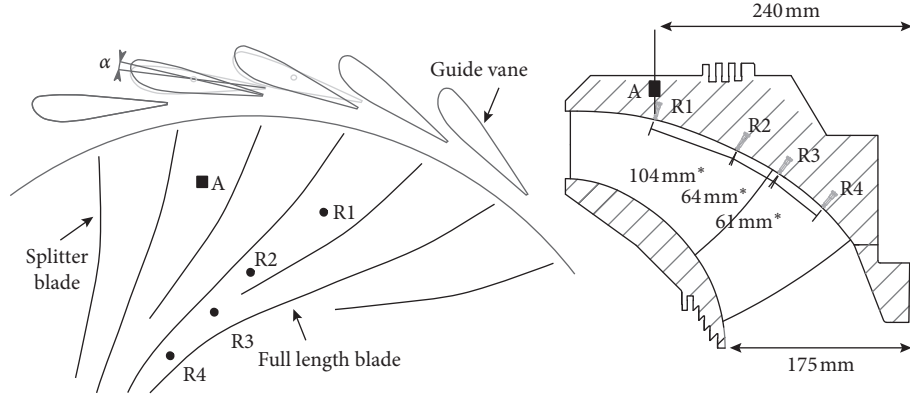


FIGURE 6: Onboard pressure sensors. The distance between the sensors is indicated. *Distance in \mathbb{R}^3 .

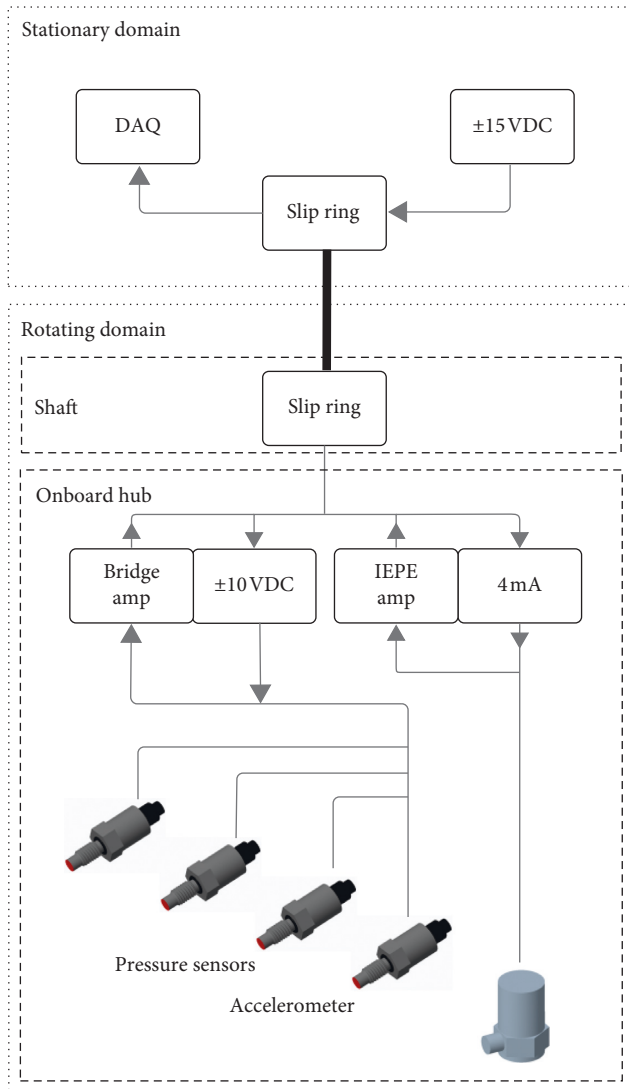


FIGURE 7: Overview of the measurement chain.

conducted at 1 Hz with a pressure alternating between 100 kPa and 90 kPa absolute pressure. The uncertainty of the amplitudes measured by the accelerometer was stated in the documentation to be relative 1%.

TABLE 1: Measurement summary.

Description	Flow (m^3/s)	n_{ED} (-)	Q_{ED} (-)	Efficiency (-)	Head (m)	α (°)	Speed (rpm)
BEP1	0.107	0.185	0.152	0.916	3.45	10.0	185.1
BEP2	0.134	0.179	0.154	0.916	5.2	10.0	219.8
BEP3	0.160	0.176	0.156	0.920	7.2	10.0	254.3
BEP4	0.183	0.178	0.154	0.919	9.6	10.0	297.8
BEP5	0.209	0.178	0.155	0.920	12.6	10.0	340.5
BEP6	0.232	0.180	0.154	0.920	15.55	10.0	381.7

α is the guide vane opening as defined in the IEC60193 where 0° is the closed position.

A vibration test with the runner surrounded by air was conducted to analyze the pressure sensors vibration sensitivity. An unbalanced mass shaker was used to excite the runner from 0 to 850 Hz. The response was measured with the accelerometer and the pressure sensors to evaluate the vibration sensitivity of the pressure sensors. Four test points were selected from the frequency response with different acceleration amplitudes and repeated with constant frequency. The results are shown in Figure 8.

The highest vibration amplitude measured by the accelerometer in the vibration test was 17 ms^{-2} . The highest measured vibration amplitude for the second harmonic of the guide vane passing frequency in the measurements BEP1 to BEP6 was 0.05 ms^{-2} in BEP6. From the results shown in Figure 8, the first comparison point was with an acceleration of 0.12 ms^{-2} while the pressure sensors response was just above the noise band, with the highest amplitudes from the sensor R4 of 0.013 kPa. The pressure sensors were measuring structural vibrations for higher acceleration values. Based on the current analysis, a conservative uncertainty estimate for the measured pressure amplitudes was $0.013 \text{ kPa} / 0.12 \text{ ms}^{-2} = 0.11 \text{ kPa/ms}^{-2}$. Assuming the unbalanced shaker excited nonrotating modes, the accuracy of the analysis was dependent on which mode was being excited and the position of the sensors relative to the diametral modes. Unfortunately, such knowledge was not available in the measurements, but since the pressure sensors had different locations and showed similar frequency sensitivity trends and the acceleration amplitudes in the measurements

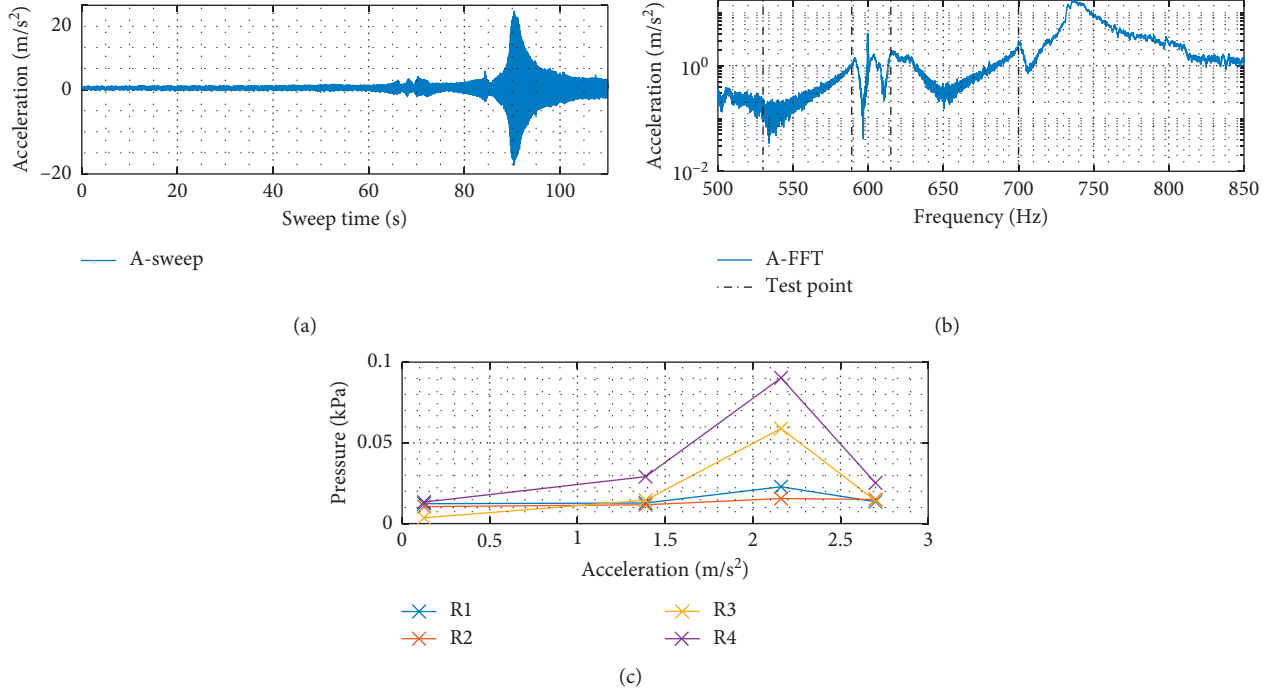


FIGURE 8: Vibration sensitivity test of the pressure sensors. The runner was excited in air with a frequency sweep with an unbalanced mass shaker. Four test points were repeated with constant frequency. The response was measured with the accelerometer and the pressure sensors.

BEP1-BEP6 were small, the analysis was assumed to be conservative and valid.

To analyze the variation of the blade-passing amplitude for each sensor, a short-time fast Fourier transform (STFFT) was used. The analysis was performed with a window length equal to 50 periods of the RSI signal with each window starting at the same relative position to the signal period. The amplitudes were found to be normally distributed, and a 95% confidence interval was calculated. The uncertainty budget for the RSI amplitudes is presented in Table 2. For the input to the pressure model, equation (9) was used to find the uncertainty in the complex domain where ε is the 95% error estimate.

$$\begin{aligned}\varepsilon_{re} &= \sin(\varphi) \cdot \varepsilon, \\ \varepsilon_{im} &= \cos(\varphi) \cdot \varepsilon.\end{aligned}\quad (9)$$

2.6. Noise Reduction. Antialiasing filters according to the Nyquist–Shannon sampling theorem were used on all measurement channels. To reduce the noise sensitivity, amplification of the measured signals was done close to the sensors inside the runner hub.

3. Results and Discussion

3.1. Measurement Results. For the accelerometer measurements, no normalization recommendations could be found in the literature. The goal of the normalization was to compare the acceleration as if the frequencies and the driving force were the same for each step in rotational speed and head. A speed ratio coefficient c was defined as the ratio

between the investigated speed, the speed of the first measurement $c = n/n_{BEP1}$, and a driving force coefficient b was defined as the ratio between investigated head and head of first measurement $b = H/H_{BEP1}$. Assuming a sinusoidal fluctuating movement $\tilde{s}(t)$,

$$\tilde{s}(t) = b \cdot \sin(c \cdot t) \quad (\text{m}). \quad (10)$$

The acceleration is

$$\frac{\partial^2 s}{\partial t^2} = \tilde{a}(t) = -b \cdot c^2 \cdot \sin(c \cdot t) \quad \left(\frac{\text{m}}{\text{s}^2}\right). \quad (11)$$

Rearranged to achieve constant acceleration amplitude independent of speed and head,

$$\tilde{a}_{nH}(t) = \frac{\tilde{a}(t)}{b \cdot c^2} = -1 \cdot \sin(c \cdot t) \quad \left(\frac{\text{m}}{\text{s}^2}\right). \quad (12)$$

The amplitudes of the fundamental guide vane passing frequency are shown in Figure 9. The pressure amplitudes show a small increasing trend which may be to some extent related to Reynolds effects [27, 28]. The IEC 60193 [21] recommends the Reynolds number (Re_{D2}) to be above $5 \cdot 10^6$ to avoid Reynolds dependencies in the model measurements. The Reynolds number range for the measurements BEP1 to BEP6 was $8 \cdot 10^5 - 2.5 \cdot 10^6$; hence, the measurements were in a range where the friction losses in the turbine were expected to be dependent of the Reynolds number. By examining the efficiency for each of the measurements in Table 1, a similar trend as the pressure amplitudes in Figure 9 is found; hence, the increased losses in the turbine at low flow could reduce the fluctuating pressure amplitudes. The accelerometer amplitudes were almost

TABLE 2: Uncertainty budget for the fundamental RSI amplitudes, BEP5.

Location	Amplitude RMS of fundamental frequency RSI	Calibration repeatability, ϵ_r	Vibration sensitivity, ϵ_v	Repeatability of the measurements, ϵ_m	Total relative uncertainty, f_t (%)
R1	0.94 kPa	0.01 kPa	0.003 kPa	0.015 kPa	1.9
R2	0.70 kPa	0.01 kPa	0.003 kPa	0.011 kPa	2.2
R3	0.53 kPa	0.006 kPa	0.003 kPa	0.010 kPa	2.3
R4	0.30 kPa	0.006 kPa	0.003 kPa	0.012 kPa	4.6
A	0.028 ms^{-2}	1%	—	0.002 m/s^{-2}	7.1

The vibration sensitivity was calculated as 0.13 times the acceleration amplitude.

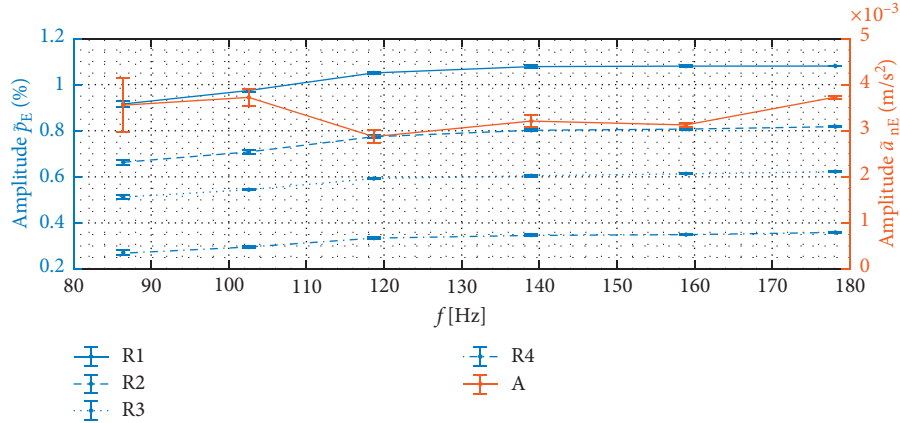


FIGURE 9: The RSI fundamental frequency. The error bars represent the uncertainty from calibration and the experimental repeatability of the amplitudes.

constant with the proposed scaling for the fundamental frequency. The excitation force from the RSI has two diametral modes for the fundamental frequency. There is no evidence of a resonance condition in the measured frequency range as presented in Figure 9.

The second harmonic of the RSI guide vane passing frequency had an increasing trend towards the measurement at 280 Hz as shown in Figure 10. The higher pressure amplitudes indicate a resonance condition. The accelerometer measurements were similar to the pressure measurements until the last measured point. The deviation on the last measured point is a clear indication of a higher mode, not visible in the pressure measurements. The number of diametral modes is four, since the forced excitation from the second harmonic of the pressure field has four diametral modes.

3.2. Fitted Model Parameters. The following steps were performed for the fitting of the measured data:

- (1) An appropriate mathematical model was selected as described in the pressure model section
- (2) A merit function was defined as the sum of square error (equation (13))
- (3) The parameters were adjusted for the best fit by minimizing the merit function with a constrained nonlinear minimizing routine
- (4) The goodness of fit was evaluated with the coefficient of determination, R^2 , and the distribution of the residuals

- (5) The accuracy of the best fit parameters was estimated with Monte Carlo simulation

The number of data points from the measurements was 60. Six measurements with 5 sensors were with amplitude and phase information. The number of model parameters was required to be less than the number of measurement to limit the degree of freedom in the fitting and avoid overfitting. The measurements were fitted to a model with convective pressure and acoustic pressure with two acoustic modes, giving 34 model parameters. The merit function was calculated as the sum of the weighted square errors as follows:

$$m = \sum_{i=1}^n w_i (y_i - \hat{y}_i)^2, \quad (13)$$

where the weights were the inverse standard deviation of the data points, $w_i = 1/\sigma^2$. The goodness of fit R^2 was calculated as shown in Table 3. The solution of the modes in the fit was restricted to be within the frequency range of the measurements.

The R^2 was relatively good for all curves, but since the analysis of R^2 cannot determine the quality of the fit, the residuals were analyzed. A good model fit should produce residuals normally distributed around zero with no systematic trends. The residuals for amplitudes and phases are shown in Figure 11. With one measurement for each sensor and a total of five points for each frequency, the distribution was not available. For accurate determination of the model fit accuracy to the measured values, more measurement points were needed. However, the residuals for the phase

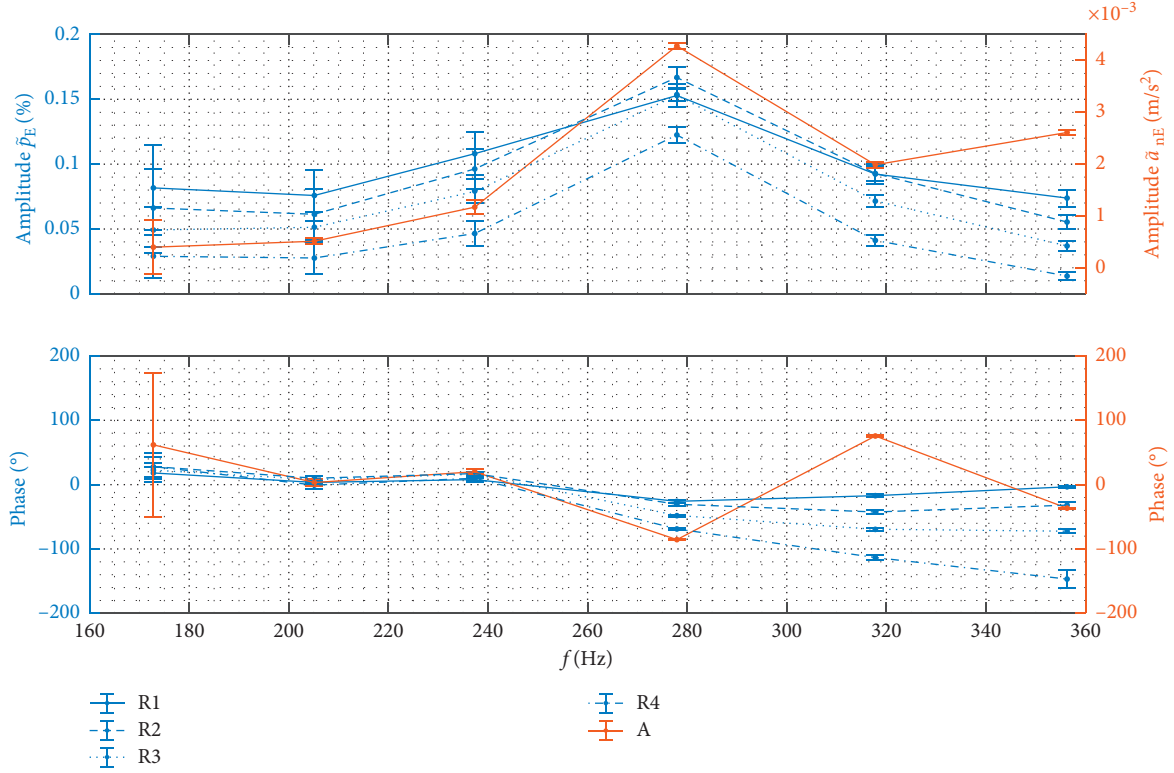


FIGURE 10: The RSI second harmonic frequency. Pressure amplitudes are normalized to the potential energy. The error bars represent the uncertainty from calibration and the experimental repeatability of the amplitudes.

TABLE 3: Goodness of fit R^2 .

	Amplitude	Phase
R1	0.903	0.933
R2	0.986	0.961
R3	0.994	0.990
R4	0.996	0.984
A	0.991	0.894

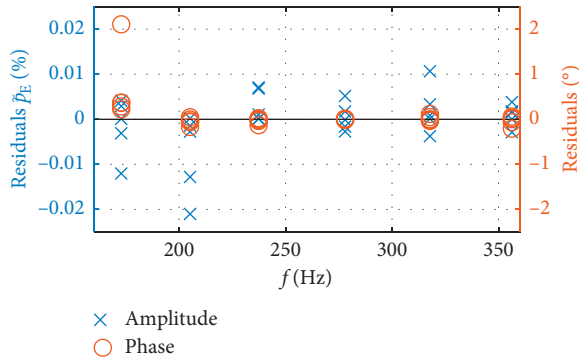


FIGURE 11: Residuals for the calculated model with two degrees of freedom in the acoustic pressure.

were, with the exception of one outlier at the first frequency, symmetrical around the zero line. The amplitude residuals were more scattered, especially for the low frequencies, but the values were relatively small. Based on the residuals, the model fitted the measurements well.

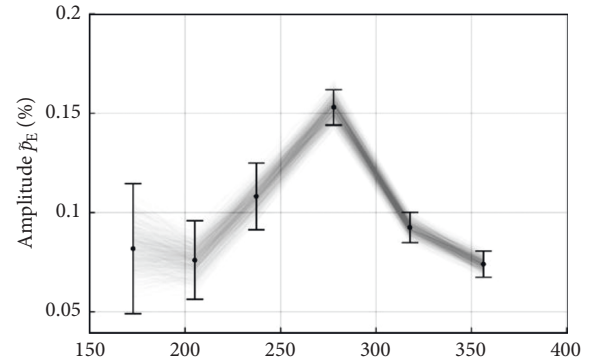


FIGURE 12: The first 1000 inputs to the MCM simulation of the amplitude data from pressure sensor R1. Each line is plotted with light color, and darker color represents coinciding lines. Measurement data are indicated.

The uncertainty of the fitting coefficients was calculated from Monte Carlo Method (MCM) simulation. The calibration uncertainties in each measurement point were not independent as required in the MCM simulation. The input to the calculation was therefore generated from normally distributed random numbers in the uncertainty interval for the calibration, combined with a normally distributed random number from the measurement uncertainty as shown in equation (14). X is a normally distributed random number, σ_c and σ_m are the standard deviation of the calibration and the measurement

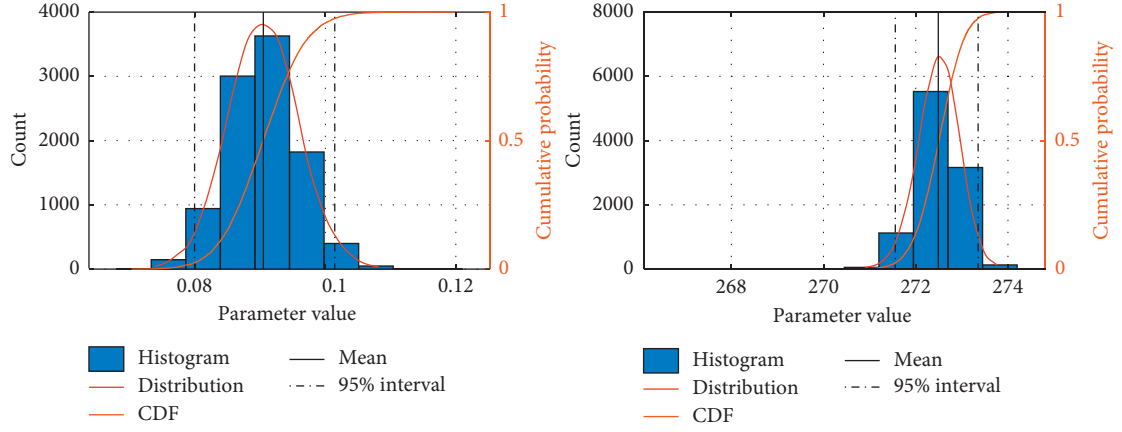


FIGURE 13: Two examples of the histogram, the distribution and the cumulative probability of the coefficients $\tilde{p}_{cRe,l}$ and ω_{n1} . Mean and 95% confidence interval are indicated.

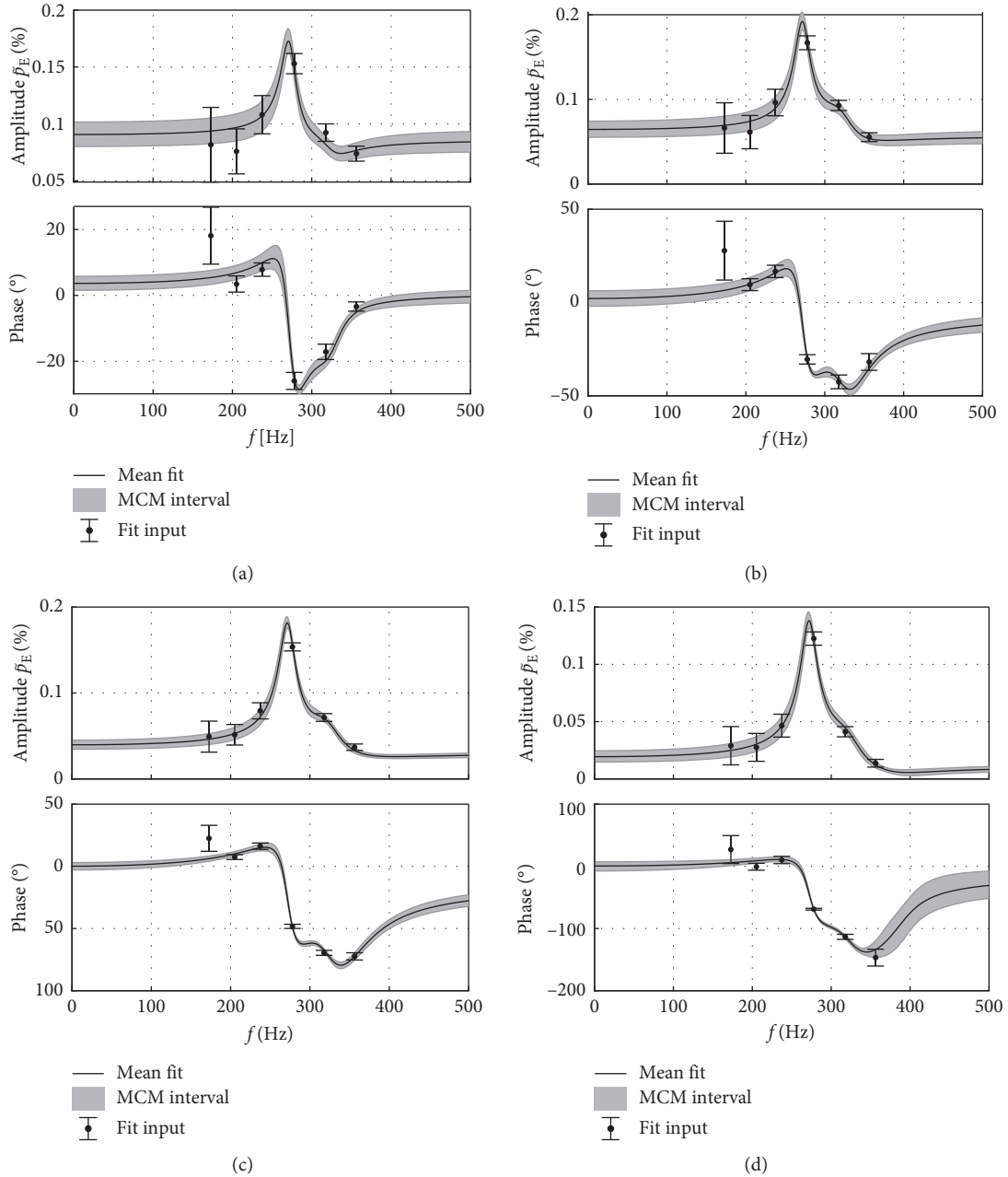


FIGURE 14: Least square fitting of the pressure measurements. (a) R1. (b) R2. (c) R3. (d) R4.

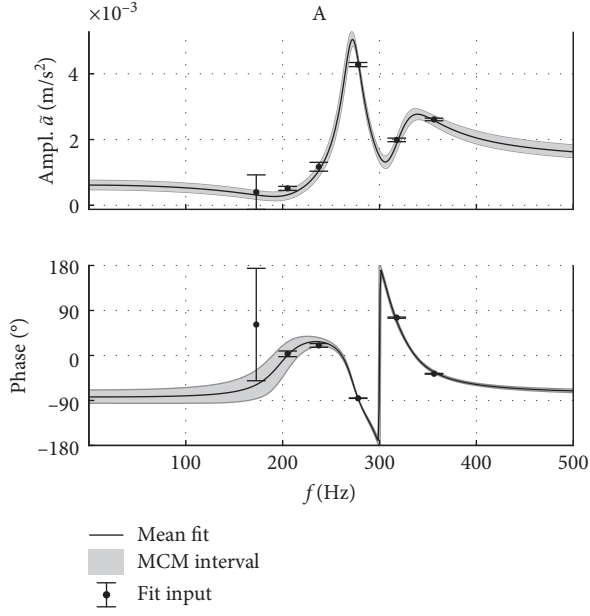


FIGURE 15: The accelerometer fit.

repeatability. The input for one iteration of the MCM simulation is shown in equation (14). The calculated range for pressure sensor R1 amplitudes with 10 000 MCM iterations is shown in Figure 12.

$$\tilde{p}_{t,jMCM} = \tilde{p}_{t,j} + (X_c \cdot \sigma_{c,j}) + [(X_m \cdot \sigma_{m,j})]_{m=BEP1}^{BEP6}. \quad (14)$$

The distribution of the coefficients from the MCM simulation was analyzed, and the 95% confidence interval was found with the empirical cumulative distribution function. Two example calculations are shown in Figure 13 for coefficients $\tilde{p}_{cRe,1}$ and ω_{n1} .

Figure 14 shows the pressure fitting results and the measured pressure data, while the accelerometer fit is shown in Figure 15. The coefficients from the fitting results are presented in Table 4 for the comparison with numerical results. For the visualization of the calculated pressure at resonance condition, the convective, acoustic1, and acoustic2 amplitudes are shown in Figure 16. The convective part of the pressure was found to diminish almost linearly relative to the distance between the sensors. The acoustic1 part of the pressure was found with highest amplitudes for R3, close to the middle of the runner channel, while the acoustic2 pressure was found with a more flat amplitude response in the runner channel.

With the use of equation (6) and $\max(\omega) = 356.25$ Hz, the damping for mode1 was found to be $\zeta_1 = 3.9 (\pm 0.4)\%$ at $\omega_{n1} = 272 (\pm 1)$ Hz, and mode2 was found to be $\zeta_2 = 7.4 (-1.2 + 1.5)\%$ at $\omega_{n2} = 326 (\pm 3)$ Hz. The accelerometer measurement was most influenced by the second mode; thus, there are reasons to believe the mode includes more disc deflection and thus possible higher damping.

The first measurement point (BEP1) had the highest uncertainty, and the proposed pressure model did not fit the phase in any of the pressure measurements, while the accelerometer model was within the range of the uncertainty.

TABLE 4: Fitting coefficients.

Description	Value and 95% interval
<i>Convective</i>	
$\tilde{p}_{cRe,1}$	0.0905 (−0.0105, 0.0109)
$\tilde{p}_{cRe,2}$	0.0644 (−0.0093, 0.0098)
$\tilde{p}_{cRe,3}$	0.0397 (−0.0051, 0.0055)
$\tilde{p}_{cRe,4}$	0.0194 (−0.0047, 0.0052)
$\tilde{a}_{c,Re}$	0.0002 (−0.0001, 0.0001)
$\tilde{p}_{cIm,1}$	0.0058 (−0.0033, 0.0033)
$\tilde{p}_{cIm,2}$	0.0024 (−0.0046, 0.0048)
$\tilde{p}_{cIm,3}$	0.0001 (−0.0020, 0.0022)
$\tilde{p}_{cIm,4}$	0.0002 (−0.0025, 0.0025)
$\tilde{a}_{c,Im}$	−0.0012 (−0.0002, 0.0002)
<i>Acoustic1</i>	
$\Phi_{Re,1}$	0.0057 (−0.0020, 0.0019)
$\Phi_{Re,2}$	0.0061 (−0.0022, 0.0021)
$\Phi_{Re,3}$	0.0111 (−0.0021, 0.0019)
$\Phi_{Re,4}$	0.0123 (−0.0021, 0.0019)
A_{Re}	0.0003 (−0.0001, 0.0000)
$\Phi_{Im,1}$	0.0099 (−0.0014, 0.0014)
$\Phi_{Im,2}$	0.0150 (−0.0018, 0.0018)
$\Phi_{Im,3}$	0.0146 (−0.0015, 0.0015)
$\Phi_{Im,4}$	0.0102 (−0.0013, 0.0014)
A_{Im}	0.0003 (0.0000, 0.0000)
<i>Acoustic2</i>	
$\Phi_{Re,1}$	0.0013 (−0.0010, 0.0011)
$\Phi_{Re,2}$	0.0053 (−0.0016, 0.0020)
$\Phi_{Re,3}$	0.0052 (−0.0013, 0.0018)
$\Phi_{Re,4}$	0.0013 (−0.0011, 0.0013)
A_{Re}	−0.0005 (−0.0001, 0.0001)
$\Phi_{Im,1}$	−0.0020 (−0.0014, 0.0011)
$\Phi_{Im,2}$	−0.0006 (−0.0014, 0.0014)
$\Phi_{Im,3}$	−0.0015 (−0.0011, 0.0009)
$\Phi_{Im,4}$	−0.0041 (−0.0017, 0.0012)
A_{Im}	0.0003 (−0.0001, 0.0001)
<i>Other</i>	
ω_{n1}	272.4895 (−0.9329, 0.8634)
$k1$	0.0510 (−0.0051, 0.0045)
ω_{n2}	325.5277 (−2.6368, 2.7486)
$k2$	0.0813 (−0.0125, 0.0153)

The amplitudes in the BEP1 were low, and also the test rig was operated at a very low head, giving the high uncertainty. For the higher frequencies, the fit was very good for all sensors giving reasons to believe the proposed model is valid. Questions can be raised about the number of measurements and the frequency step, and the accuracy would likely be better. The analysis method can separate experimental pressure data into convective and acoustic pressure. The convective pressure represents the pressure field not influenced by the vibrating structure, while the acoustic pressure represents the pressure from the fluid structure interaction.

4. Conclusion

The pressure measurements were able to find a resonance, and the proposed pressure model was able to calculate the convective and acoustic parts of the pressure for the investigated runner. By separating the measured pressure amplitudes into an acoustic and a convective pressure field, their individual shapes together with the eigenfrequency and

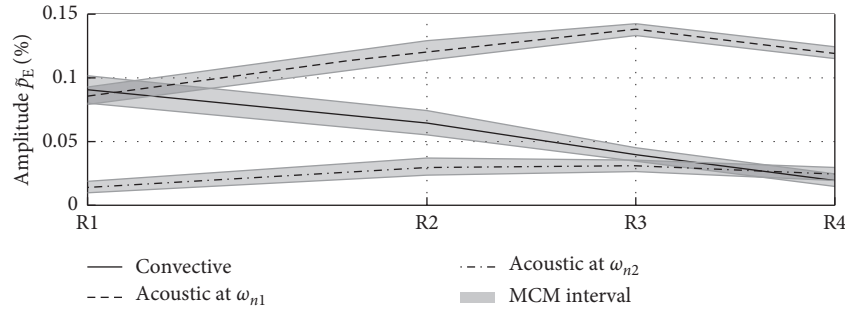


FIGURE 16: The calculated amplitudes from the fitting coefficients in Table 4 for R1–R4. The distance between the sensors is according to Figure 6.

the damping were estimated. The convective pressure field diminishes almost linearly from the inlet to the outlet, while the acoustic pressure field had the highest amplitudes in the middle of the runner channel. At resonance, the acoustic pressure clearly dominates over the convective. For the acoustic1 mode, the estimated eigenfrequency was 272 Hz while the damping was in the range of 2.5% to 5.1% depending on the runner speed. The acoustic2 mode was estimated to 326 Hz with the damping in the range of 4% to 8%. It is shown that the analysis method can separate experimental data corresponding to the different results of numerical analyses. The convective pressure represents the output from computational fluid dynamics (CFD), and the acoustic pressure, resonance frequency, and damping represent the output from simulations as modal and flutter analysis.

Abbreviations

2DOF: Two degrees of freedom
 Amp: Amplifier
 BEP: Best efficiency point
 CFD: Computation fluid dynamics
 DAQ: Data acquisition
 IEC: International Electrotechnical Commission
 IEPE: Integrated Electronics Piezo-Electric
 MCM: Monte Carlo method
 DM: Diametral mode
 RSI: Rotor-stator interaction
 STFFT: Short-Time fast Fourier transform
 VDC: Volt direct current.

Nomenclature

A: Accelerometer mode
 α : Guide vane opening
 \tilde{a} : Fluctuating acceleration
 ε_r : 95% repeatability from calibration
 ε_v : 95% vibration sensitivity
 ε_m : 95% repeatability of the measurements
 ε_t : 95% total uncertainty
 ζ : Damping coefficient
 σ : Standard deviation
 σ_r : Standard deviation of the calibration
 σ_m : Standard deviation of the measurement
 Φ : Acoustic pressure mode

ω : Frequency
 ω_p : Frequency proportionality
 H : Head of machine
 k : Damping proportionality constant
 n_{ED} : Dimensionless speed factor
 \tilde{p} : Fluctuating pressure
 Q_{ED} : Dimensionless discharge.

Subscripts for the pressure symbols

a : Acoustic pressure
 c : Convective pressure
 E : Specific hydraulic energy of machine
 j : Sensor identification
 Im : Imaginary part
 Re : Real part
 t : Total pressure.

Data Availability

The measurement data and geometry used to support the findings of this study are available at the Francis-99 website [28].

Conflicts of Interest

The authors declare that they have no conflicts of interest.

Acknowledgments

The experiments were conducted under the HiFrancis research project. The authors are grateful for all the support from the technical staff at the Waterpower laboratory to make the measurements possible. This work was funded by Energy Norway, Norwegian Research Council, and the Norwegian Hydropower Center.

References

- [1] P. T. K. Østby, J. T. Billdal, K. Sivertsen, B. Haugen, and O. G. Dahlhaug, "Dynamic stresses in high head francis turbines," *Hydropower Dams*, vol. 3, 2016.
- [2] A. Presas, D. Valentin, E. Egusquiza, C. Valero, M. Egusquiza, and M. Bossio, "Accurate determination of the frequency response function of submerged and confined structures by using PZT-patches†," *Sensors*, vol. 17, no. 3, p. 660, 2017.

- [3] H. Tanaka, "Vibration behavior and dynamic stress of runners of very high head reversible pump-turbines," *International Journal of Fluid Machinery and Systems*, vol. 4, no. 2, pp. 289–306, 2011.
- [4] C. G. Rodriguez, E. Egusquiza, and I. F. Santos, "Frequencies in the vibration induced by the rotor stator interaction in a centrifugal pump turbine," *Journal of Fluids Engineering*, vol. 129, no. 11, p. 1428, 2007.
- [5] Y. Kubota, T. Susuki, H. Tomita, T. Nagafugi, and C. Okamura, "Vibration of rotating bladed disc excited by stationary distributed forces," *Bulletin of JSME*, vol. 26, no. 221, pp. 1952–1957, 1983.
- [6] C. G. Rodriguez, B. Mateos-Prieto, and E. Egusquiza, "Monitoring of rotor-stator interaction in pump-turbine using vibrations measured with on-board sensors rotating with shaft," *Shock and Vibration*, vol. 2014, Article ID 276796, 8 pages, 2014.
- [7] L. Bertini, P. Neri, C. Santus, A. Guglielmo, and G. Mariotti, "Analytical investigation of the SAFE diagram for bladed wheels, numerical and experimental validation," *Journal of Sound and Vibration*, vol. 333, no. 19, pp. 4771–4788, 2014.
- [8] D. Valentín, D. Ramos, M. Bossio, A. Presas, E. Egusquiza, and C. Valero, "Influence of the boundary conditions on the natural frequencies of a Francis turbine," *IOP Conference Series: Earth and Environmental Science*, vol. 49, no. 7, article 072004, 2016.
- [9] A. Presas, C. Valero, X. Huang, E. Egusquiza, M. Farhat, and F. Avellan, "Analysis of the dynamic response of pump-turbine runners-Part I: Experiment," *IOP Conference Series: Earth and Environmental Science*, vol. 15, no. 5, article 052015, 2012.
- [10] P. T. K. Østby, K. Sivertsen, J. T. Billdal, and B. Haugen, "Experimental investigation on the effect off near walls on the eigen frequency of a low specific speed francis runner," *Mechanical Systems and Signal Processing*, vol. 118, pp. 757–766, 2019.
- [11] D. Valentín, A. Presas, M. Bossio, M. Egusquiza, E. Egusquiza, and C. Valero, "Feasibility of detecting natural frequencies of hydraulic turbines while in operation, using strain gauges," *Sensors*, vol. 18, no. 2, p. 174, 2018.
- [12] S. Lais, Q. Liang, U. Henggeler, T. Weiss, X. Escaler, and E. Egusquiza, "Dynamic analysis of francis runners—experiment and numerical simulation," *International Journal of Fluid Machinery and Systems*, vol. 2, no. 4, pp. 303–314, 2009.
- [13] S. Kurosawa, K. Matsumoto, J. Miyagi, L. He, and Z. Wang, "Fluid-structure interaction analysis for resonance investigation of pump-turbine runner," in *Proceedings of ASME/JSME/KSME 2015 Joint Fluids Engineering Conference part 2*, vol. 1A: Symposia, p. V01AT12A002, Seoul, South Korea, 2015.
- [14] F. Kushner, "Rotating component modal analysis and resonance avoidance recommendations," in *Proceeding of the Thirty-Third Turbomachinery Symposium*, pp. 143–162, Houston, TX, USA, 2004.
- [15] E. Egusquiza, C. Valero, Q. Liang, M. Coussirat, and U. Seidel, "Fluid added mass effect in the modal response of a pump-turbine impeller," in *Proceedings of ASME 2009 International Design Engineering Technical Conferences and Computers and Information in Engineering Conference*, pp. 715–724, San Diego, CA, USA, August–September 2009.
- [16] C. G. Rodriguez, E. Egusquiza, X. Escaler, Q. W. Liang, and F. Avellan, "Experimental investigation of added mass effects on a Francis turbine runner in still water," *Journal of Fluids and Structures*, vol. 22, no. 5, pp. 699–712, 2006.
- [17] D. Valentín, A. Presas, E. Egusquiza, C. Valero, and M. Bossio, "Dynamic response of the MICA runner. Experiment and simulation," *Journal of Physics: Conference Series*, vol. 813, no. 1, article 012036, 2017.
- [18] Francis-99 NTNU, 2018, <https://www.ntnu.edu/nvks/francis-99>.
- [19] Ø. Antonsen, "Unsteady flow in wicket gate and runner with focus on static and dynamic load on runner," Doctoral thesis, Norwegian University of Science and Technology, Trondheim, Norway, 2007.
- [20] J. M. Tyler and T. G. Sofrin, *Axial Flow Compressor Noise Studies*, SAE International, Warrendale, PA, USA, 1962.
- [21] IEC, *NEK IEC 60193 Hydraulic turbines, Storage Pumps and Pump-Turbines Model Acceptance Tests*, International Electrotechnical Commission, Geneva, Switzerland, 1999.
- [22] R. E. Rayle, "An investigation of the influence of orifice geometry on static pressure measurements," Master thesis, Massachusetts Institute of Technology, Cambridge, MA, USA, 1949.
- [23] R. E. Franklin and J. M. Wallace, "Absolute measurements of static-hole error using flush transducers," *Journal of Fluid Mechanics*, vol. 42, no. 1, pp. 33–48, 1970.
- [24] J. P. Hessling, "A novel method of estimating dynamic measurement errors," *Measurement Science and Technology*, vol. 17, no. 10, pp. 2740–2750, 2006.
- [25] C. W. Bergan, B. W. Solemslie, P. Østby, and O. G. Dahlhaug, "Hydrodynamic damping of a fluttering hydrofoil in high-speed flows," *International Journal of Fluid Machinery and Systems*, vol. 11, no. 2, pp. 146–153, 2018.
- [26] P. F. Dunn, *Measurement and Data Analysis for Engineering and Science*, CRC Press, Boca Raton, FL, USA, 3rd edition, 2014.
- [27] T. Ida, "Analysis of scale effects on performance characteristics of hydraulic turbines," *Journal of Hydraulic Research*, vol. 28, no. 1, pp. 93–104, 1990.
- [28] P. T. K. Østby, J. T. Billdal, B. Haugen, and O. G. Dahlhaug, "On the relation between friction losses and pressure pulsations caused by Rotor Stator interaction on the Francis-99 turbine," *Journal of Physics: Conference Series*, vol. 782, no. 1, article 012010, 2017.

